PNAS RESEARCH ARTICLE | MICROBIOLOGY OPEN ACCESS

SARS-CoV-2 couples evasion of inflammatory response to activated nucleotide synthesis

Chao Qin[a], Youliang Rao[a], Hao Yuan[a,b], Ting-Yu Wang[a], Jun Zhao[a,c], Bianca Espinosa[b], Yongzhen Liu[a], Shu Zhang[a], Ali Can Savas[a], Qizhi Liu[a], Mehrnaz Zarinfar[a], Stephanie Rice[a], Jill Henley[d], Lucio Comai[d], Nicholas A. Graham[e], Casey Chen[a], Chao Zhang[b], and Pinghui Feng[a,1]

Edited by Peter Palese, Icahn School of Medicine at Mount Sinai, New York, NY; received December 19, 2021; accepted April 8, 2022

Severe acute respiratory syndrome coronavirus 2 (SARS-CoV-2) evolves rapidly under the pressure of host immunity, as evidenced by waves of emerging variants despite effective vaccinations, highlighting the need for complementing antivirals. We report that targeting a pyrimidine synthesis enzyme restores inflammatory response and depletes the nucleotide pool to impede SARS-CoV-2 infection. SARS-CoV-2 deploys Nsp9 to activate carbamoyl-phosphate synthetase, aspartate transcarbamoylase, and dihydroorotase (CAD) that catalyzes the rate-limiting steps of the de novo pyrimidine synthesis. Activated CAD not only fuels de novo nucleotide synthesis but also deamidates RelA. While RelA deamidation shuts down NF-κB activation and subsequent inflammatory response, it up-regulates key glycolytic enzymes to promote aerobic glycolysis that provides metabolites for de novo nucleotide synthesis. A newly synthesized small-molecule inhibitor of CAD restores antiviral inflammatory response and depletes the pyrimidine pool, thus effectively impeding SARS-CoV-2 replication. Targeting an essential cellular metabolic enzyme thus offers an antiviral strategy that would be more refractory to SARS-CoV-2 genetic changes.

SARS-CoV-2 | metabolism | inflammatory response | CAD | deamidation

Significance

Severe acute respiratory syndrome coronavirus 2 (SARS-CoV-2) has caused the global COVID-19 pandemic. Although ongoing vaccination drastically reduces SARS-CoV-2 infection, mutant viruses are emerging under the pressure of neutralizing antibodies, calling for new antiviral strategies. Here, we report that SARS-CoV-2 couples evasion of inflammatory response to activated nucleotide synthesis. Inhibition of a key metabolic enzyme not only depletes the nucleotide pool but also restores host inflammatory defense, thereby effectively impeding SARS-CoV-2 replication. Targeting cellular enzymes offers an avenue to combat rapidly evolving SARS-CoV-2 variants.

Having emerged in December 2019, the severe acute respiratory syndrome coronavirus 2 (SARS-CoV-2) has caused a global pandemic with more than 437 million infections and 5.96 million deaths as of March 1, 2022, not to mention unknown asymptomatic infections (https://coronavirus.jhu.edu/). Although closely related to the previously emerged SARS-CoV and Middle East respiratory syndrome CoV, SARS-CoV-2 is astonishingly transmissible and infectious in humans (1, 2). The molecular mechanisms underlying these epidemiological phenotypes of SARS-CoV-2 are emerging from studies that examine the viral entry step mediated by the viral spike protein and its human ACE2 receptor. In addition to the viral entry, intracellular events involving viral replication and host response are expected to contribute to SARS-CoV-2 pathogenesis, although our understanding concerning how SARS-CoV-2 adapts to and exploits cellular processes remains rudimentary at best.

As obligate intracellular pathogens, viruses rely on cellular mechanisms that power the biosynthesis of various components essential for progeny production, including nucleic acids, proteins, and lipids (3–5). Central to the biomass accumulation and virion reproduction, nucleotide synthesis produces materials for transcription, translation, genome replication, assembly, and egress of the viral productive infection cycle (6, 7). Importantly, UDP is required for the synthesis of glycoproteins that mediate viral entry during a new cycle of infection (8–10). Similar to proliferating cells, viruses activate anabolic pathways to accumulate biomass in preparation for viral replication (4, 5, 11–13). Although most of the metabolic pathways are known to be crucial for effective viral productive infection, how exactly viruses manipulate, explore, and exploit these pathways to program cellular metabolism and promote viral replication remains largely obscure.

The highly transmissible nature of SARS-CoV-2 in humans rests, at least partly, on efficient viral entry mediated by an enhanced interaction between the spike protein and a human ACE2 receptor (14–18). Cellular metabolism and innate immune response are two processes that potentially influence viral replication downstream of the entry step. To probe the immune evasion of cytokine production in SARS-CoV-2 infection, we discovered that SARS-CoV-2 activates de novo pyrimidine synthesis via the rate-limiting enzyme, carbamoyl phosphate synthetase, aspartate transcarbamoylase, and dihydroorotase (CAD). Activated CAD not only fueled de novo nucleotide synthesis but also nullified antiviral inflammatory response, thus coupling evasion of inflammatory response to metabolic activation. A screen identified that SARS-CoV-2 Nsp9 was sufficient to activate CAD for nucleotide synthesis and evasion of inflammatory

Author contributions: C.Q., H.Y., C.Z., and P.F. designed research; C.Q., Y.R., H.Y., T.-Y.W., J.Z., B.E., Y.L., S.Z., A.C.S., M.Z., S.R., and J.H. performed research; C.Q., Y.R., Q.L., L.C., and N.A.G. contributed new reagents/analytic tools; C.Q., H.Y., T.-Y.W., J.Z., S.Z., A.C.S., N.A.G., C.C., C.Z., and P.F. analyzed data; and C.Q., C.Z., and P.F. wrote the paper.

Competing interest statement: P.F., C.Q., C.Z., H.Y., Y.R., T.Y.W., and A.C.S. have a pending patent on the small-molecule inhibitor of CAD.

This article is a PNAS Direct Submission.

[1]To whom correspondence may be addressed. Email: pinghuif@usc.edu.

This article contains supporting information online at http://www.pnas.org/lookup/suppl/doi:10.1073/pnas.2122897119/-/DCSupplemental.

Published June 14, 2022.

response. As such, a de novo synthesized small-molecule inhibitor of CAD depleted nucleotides and restored antiviral inflammatory response, thereby effectively impeding SARS-CoV-2 replication. Such inhibitors targeting essential cellular enzymes represent new antiviral modalities that would circumvent the emerging genetic change of SARS-CoV-2 featuring the ongoing COVID-19 pandemic.

Results

SARS-CoV-2 Suppresses Inflammatory Response via Inducing RelA Deamidation. To probe the inflammatory response against SARS-CoV-2, we compared the expression of NF-κB genes induced by SARS-CoV-2 to that by Sendai virus, a prototype RNA virus. In normal human bronchial epithelial (NHBE) cells which show immune response to respiratory viruses (19), SARS-CoV-2 infection induced a weak and delayed expression of NF-κB–responsive genes, including *TNFA, IL-8, NFKB1A, CXCL10*, and *CCL5* (Fig. 1*A*). In stark contrast, Sendai virus triggered a rapid and robust expression of these genes, with a peak at 6 h postinfection (hpi) (Fig. 1*A*). Similar patterns in fold and kinetics of induction were observed in human Calu-3 lung cancer cells upon SARS-CoV-2 infection (*SI Appendix*, Fig. S1*A*). To query whether SARS-CoV-2 infection inhibits NF-κB, we sequentially infected Calu-3 and NHBE cells with SARS-CoV-2 and Sendai virus, and determined the expression of NF-κB–responsive genes. To ensure every cell infected with Sendai virus is also infected with SARS-CoV-2, we infected cells with SARS-CoV-2 at a multiplicity of infection (MOI) of 5. SARS-CoV-2 infection in Calu-3 and NHBE cells was evaluated by using an mNeonGreen-marked SARS-CoV-2 (icSARS-CoV-2-mNG) (*SI Appendix*, Fig. S2 *A* and *B*). We found that SARS-CoV-2 infection significantly reduced the expression of NF-κB–responsive genes induced by Sendai virus (Fig. 1*B* and *SI Appendix*, Fig. S1*B*). These results support the conclusion that SARS-CoV-2 inhibits the expression of NF-κB–dependent antiviral genes.

RelA is a transcriptionally active component of NF-κB; we were keen on its deamidation that can efficiently shut down inflammatory gene expression (20). Thus, we examined whether SARS-CoV-2 infection induces RelA deamidation. Indeed, in Caco-2 cells, SARS-CoV-2 infection shifted RelA toward the positive end of the gel strips, as analyzed by two-dimensional gel electrophoresis (2-DGE), consistent with the outcome of deamidation (Fig. 1*C* and *SI Appendix*, Fig. S1*C*). SARS-CoV-2 showed high infection rates at early time points (24 and 48 hpi) with MOI = 5 or late time points (72 and 96 hpi) with MOI = 0.1 in Caco-2 cells (*SI Appendix*, Fig. S2 *C* and *D*). We have previously reported that RelA can be deamidated at N64 and N139 (20). The deamidated RelA-DD (containing N64D and N139D) and deamidation-resistant RelA-N64A mediate aerobic glycolysis and inflammatory response via transcriptional regulation, respectively. Thus, we used primary mouse embryonic fibroblasts (MEFs) isolated from RelA-DD and RelA-N64A knock-in mice to analyze NF-κB response upon SARS-CoV-2 infection. To facilitate SARS-CoV-2 infection, we established MEF cell lines stably expressing human ACE2 (hACE2) (*SI Appendix*, Figs. S1*D* and S2*E*). Real-time PCR analysis showed that wild-type RelA modestly and RelA-N64A more robustly induced the expression of *Il8*, *Cxcl1*, and *Tnfa*, while RelA-DD failed to do so (Fig. 1*D*). We further analyzed RelA deamidation in wild-type and RelA-N64A MEFs after SARS-CoV-2 infection. Viral infection obviously shifted wild-type RelA to the positive end of the gel strip, while having no effect on RelA-N64A in MEFs (Fig. 1*E*). To probe the role of RelA deamidation in SARS-CoV-2 replication, we analyzed viral RNA levels and titer. Compared to wild-type RelA, RelA-DD markedly increased, while RelA-N64A reduced, SRAS-CoV-2 replication (*SI Appendix*, Fig. S1 *E* and *F*). These results support the conclusion that SARS-CoV-2 induces RelA deamidation to promote its replication.

To probe the in vivo role of RelA deamidation in SARS-CoV-2 replication, we used RelA-N64A knock-in mice for SARS-CoV-2 infection. To enable SARS-CoV-2 infection, we transduced C57BL/6 mice with adeno-associated virus (AAV) expressing hACE2 (21). Once hACE2 expression was validated, we evaluated inflammatory gene expression in AAV-hACE mice (*SI Appendix*, Fig. S1*G*). Real-time PCR analysis showed that SARS-CoV-2 induced a moderate expression of inflammatory cytokines peaking at 4 d postinfection (dpi) to 6 dpi (*SI Appendix*, Fig. S1*H*). When infected with SARS-CoV-2, RelA-N64A mice expressed NF-κB–dependent genes at levels that were approximately twofold to sevenfold those in wild-type mice at 4 dpi (Fig. 1*F*). Conversely, plaque assays using lung lysates showed that SARS-CoV-2 titer in RelA-N64A mice was more than two orders of magnitude lower than that in wild-type mice (Fig. 1*G*). Consistent with this, RelA-N64A also reduced the abundance of SARS-CoV-2 RNA by ∼1.5 orders of magnitude (*SI Appendix*, Fig. S1*I*). These results collectively support the conclusion that SARS-CoV-2 induces RelA deamidation to inhibit NF-κB activation and promote viral replication.

To determine whether CAD is required for SARS-CoV-2–induced RelA deamidation, we depleted CAD in Caco-2 cells and examined RelA deamidation upon SARS-CoV-2 infection. In control cells, the more negatively charged species was increased after SARS-CoV-2 infection, indicative of induced deamidation (*SI Appendix*, Fig. S3*A*). Moreover, CAD depletion abolished SARS-CoV-2–induced RelA deamidation (*SI Appendix*, Fig. S3*A*). We previously validated the specificity of CAD in RelA deamidation using CAD-knockout cells and two pairs of short hairpin RNA (shRNA) (20); we thus depleted CAD with one shRNA and examined antiviral gene expression upon SARS-CoV-2 infection. Remarkably, CAD depletion in NHBE cells elevated the expression of antiviral genes by an order of magnitude upon SARS-CoV-2 infection, including those of *CXCL1*, *CXCL2*, *CCL2*, and *NFKB1A* (Fig. 1*H*). Similarly, CAD depletion in Calu-3 cells elevated the expression of these genes upon SARS-CoV-2 infection (*SI Appendix*, Fig. S3*B*). These results demonstrate that CAD is crucial for RelA deamidation and inhibition of inflammatory cytokine production during SARS-CoV-2 infection.

SARS-CoV-2 Nsp9 Activates CAD to Inhibit NF-κB Activation. To probe the virus–host interaction underpinning SARS-CoV-2–induced RelA deamidation, we screened for viral proteins that interact with CAD, using a SARS-CoV-2 expression library (22). Affinity purification followed by immunoblotting analysis identified multiple SARS-CoV-2 polypeptides, including Nsp8, Nsp9, ORF7a, ORF8, M, and ORF10, that coprecipitated with endogenous CAD in HEK293T cells expressing SARS-CoV-2 proteins (Fig. 2*A*). Because CAD deamidates RelA to block NF-κB activation (20), we further assessed whether these CAD-binding proteins inhibit NF-κB activation by a luciferase reporter assay. When NF-κB activation was induced with overexpressed MAVS, we found that only Nsp9, out of all six SARS-CoV-2 polypeptides, modestly reduced NF-κB activation (Fig. 2*B*). Given that ORF10 expression was low, we further performed reporter assays and found that ORF10 reduced NF-κB activation induced by

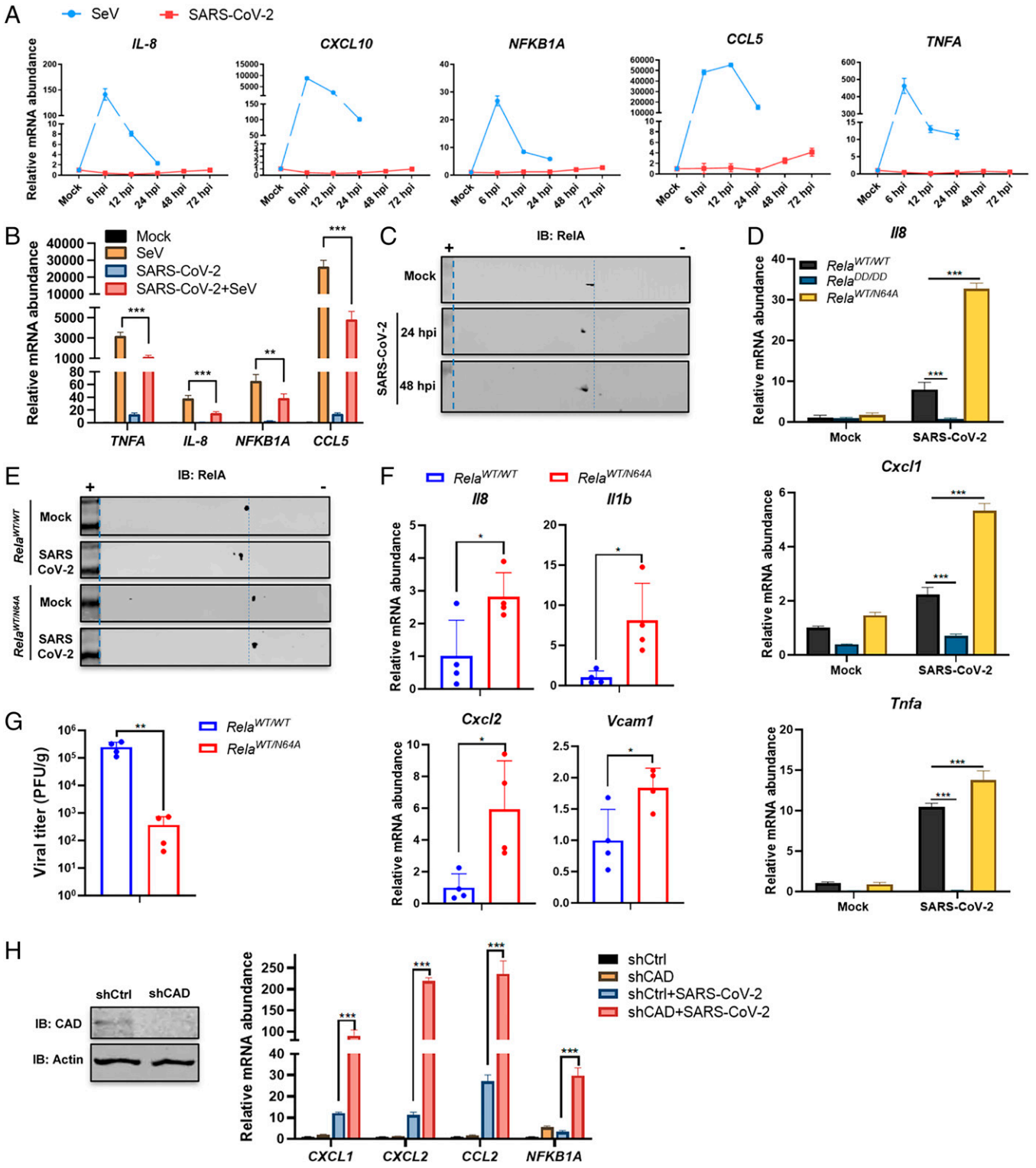

Fig. 1. SARS-CoV-2 inhibits cytokines production via inducing RelA deamidation. (*A*) NHBE cells were infected with SARS-CoV-2 (MOI = 0.1) or Sendai virus (SeV, 100 HAU/mL) for the indicated time. Total RNA was extracted and analyzed by real-time PCR with primers specific for indicated genes. (*B*) Calu-3 cells were mock infected or infected with SARS-CoV-2 (MOI = 5) for 24 h and superinfected with SeV (100 hemagglutination units (HAU)/mL) for 6 h. The expression of the indicated genes was analyzed by real-time PCR using total RNA. (*C*) Caco-2 cells were mock infected or infected with SARS-CoV-2 (MOI = 5) for 24 and 48 h. WCLs were analyzed by 2-DGE and immunoblotting. (*D*) RelA wild-type, RelA-DD, and RelA-N64A knock-in MEFs expressing human ACE2 (hACE2) were infected with SARS-CoV-2 (MOI = 0.1) for 24 h. The expression of indicated genes was analyzed by real-time PCR. (*E*) RelA wild-type and RelA-N64A knock-in MEFs expressing hACE2 were infected with SARS-CoV-2 (MOI = 0.1) for 24 h. WCLs were analyzed by 2-DGE and immunoblotting. (*F* and *G*) AAV-hACE2 transduced wild-type and RelA-N64A knock-in mice ($n = 4$) were intranasally infected with SARS-CoV-2 (5×10^5 pfu). The expression of cytokine genes (*F*) and viral titer (*G*) in the lung were determined by real-time PCR and plaque assay, respectively. (*H*) NHBE cells were infected with control lentivirus or lentivirus carrying shRNA against CAD. Cells were then infected with SARS-CoV-2 (MOI = 0.5) for 24 h. WCLs were analyzed by immunoblotting with indicated antibodies, and the expression of inflammatory genes was analyzed by real-time PCR. Data are presented as means ± SD of biological triplicates (*A, B, D,* and *H*) and are representative of three independent experiments (*C* and *E*). In *F* and *G*, four mice were used in each group. Statistical analysis was performed by the two-way ANOVA test, one-way ANOVA test, or unpaired, two-tailed Student's *t* test. $^*P < 0.05$; $^{**}P < 0.01$; $^{***}P < 0.001$.

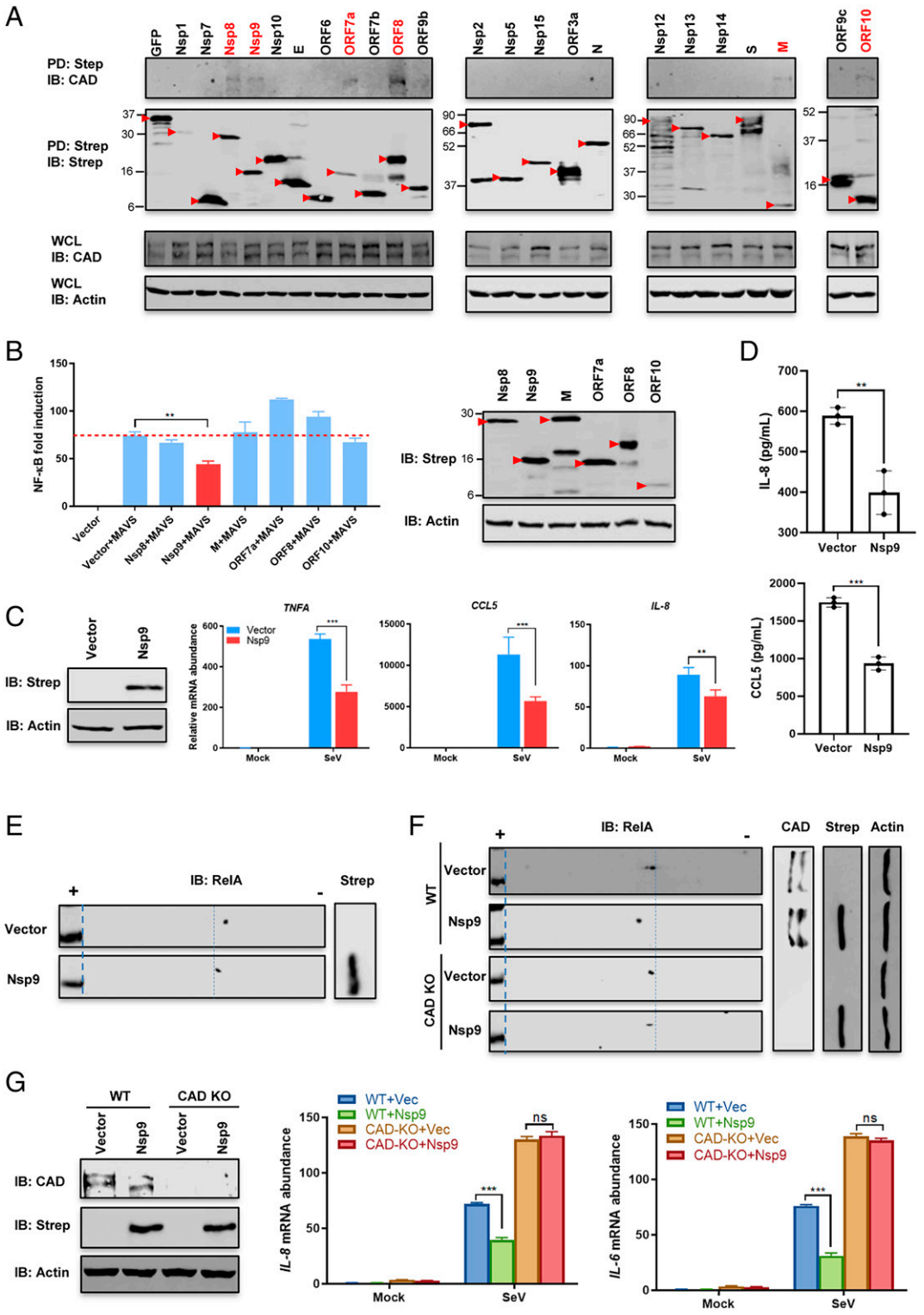

Fig. 2. SARS-CoV-2 Nsp9 inhibits NF-κB activation through CAD. (*A*) HEK293T cells were transfected with plasmids expressing Strep-tagged GFP or SARS-CoV-2 viral proteins. At 48 h posttransfection, WCLs were incubated with StrepTactin beads. WCLs and precipitated proteins were analyzed by immunoblotting with indicated antibodies. Red arrowheads indicate viral proteins. (*B*) HEK293T cells were transfected with plasmids expressing MAVS or SARS-CoV-2 polypeptides, and NF-κB luciferase reporter plasmid mixture. Luciferase activity was determined at 24 h after transfection. (*C*) NHBE cells were infected with control lentivirus or that carrying Nsp9. At 72 hpi, cells were infected with SeV (100 HAU/mL) for 6 h. Total RNA was extracted and analyzed by real-time PCR with primers specific for indicated genes. (*D*) Nsp9-expressed or control NHBE cells were infected with SeV (100 HAU/mL) for 12 h. IL-8 and CCL5 protein levels in the supernatants were determined by ELISA. (*E*) Caco-2 cells were infected with control lentivirus or that carrying Nsp9. At 72 hpi, cells were harvested, and WCLs were analyzed by 2-DGE and immunoblotting with indicated antibodies. (*F*) Wild-type (WT) and CAD-knockout HCT116 cells were infected with control lentivirus or that carrying Nsp9. At 72 hpi, WCLs were analyzed by 2-DGE and immunoblotting with indicated antibodies. (*G*) Wild-type and CAD-knockout HCT116 cells were infected with control lentivirus or that containing Nsp9. At 72 hpi, cells were infected with SeV (100 HAU/mL) for 6 h. WCLs were analyzed by immunoblotting with indicated antibodies, and the expression of indicated genes was analyzed by real-time PCR. Data are presented as means ± SD of biological triplicates (*B, C, D,* and *G*) and are representative of three independent experiments (*A, E,* and *F*). Statistical analysis was performed by the two-way ANOVA test, one-way ANOVA test, or unpaired, two-tailed Student's *t* test. $^{**}P < 0.01$; $^{***}P < 0.001$; ns, not significant.

MAVS overexpression, but not that by RelA overexpression, in a dose-dependent manner (*SI Appendix*, Fig. S3 *C* and *D*). The inhibition of MAVS by ORF10 was consistent with what was previously reported (23), while ORF7a had no detectable effect (*SI Appendix*, Fig. S3*E*). We then established an NHBE cell line that stably expresses Nsp9 and examined innate immune activation upon Sendai virus infection. Real-time PCR analysis indicated that Nsp9 inhibited the expression of NF-κB–responsive genes, such as *TNFA*, *CCL5*, and *IL-8*, induced by Sendai virus infection (Fig. 2*C*). This was further confirmed by reduced CCL5 and IL-8 in the medium as analyzed by ELISA (Fig. 2*D*). To probe the mechanism of down-regulation of NF-κB, we analyzed RelA deamidation by 2-DGE and found that Nsp9 shifted RelA toward the positive end of the gel strip, indicative of deamidation (Fig. 2*E* and *SI Appendix*, Fig. S3*F*). Moreover, loss of CAD abolished the shift of RelA induced by Nsp9 in HCT116 cells, supporting the conclusion that Nsp9 induces CAD-mediated RelA deamidation (Fig. 2*F*). We expressed Nsp9 in RelA-WT and RelA-DD HCT116 cells and found that Nsp9 shifted only RelA-WT toward the positive end of the gel strip, but not RelA-DD, in HCT116 cells (*SI Appendix*, Fig. S3*G*). To determine the role of CAD in the down-regulation of NF-κB activation by Nsp9, we employed CAD-knockout HCT116 cells to analyze innate inflammatory gene expression. Indeed, Nsp9 inhibited the expression of *IL-8* and *IL-6* in wild-type HCT116 cells, while having no effect in CAD-knockout HCT116 cells, in response to Sendai virus infection (Fig. 2*G*). Collectively, these results show that Nsp9 inhibits NF-κB activation through CAD-mediated RelA deamidation.

SARS-CoV-2 Activates CAD to Promote Replication. CAD catalyzes the first three steps of the de novo pyrimidine synthesis pathway, with the first step being rate limiting (Fig. 3*A*). Thus, CAD is crucial for de novo nucleotide synthesis that underpins cell proliferation and virus replication (24–26). The activity of CAD in synthesizing pyrimidine is up-regulated by phosphorylation of serine 1859 (S1859) mediated by the ribosomal protein S6 kinase 1 (S6K1) (27–29). We analyzed the S1859 phosphorylation of CAD in cells infected with SARS-CoV-2. Immunoblotting analysis indicated that the level of phosphorylated S1859 of CAD was significantly higher in SARS-CoV-2–infected cells compared to mock-infected cells (Fig. 3*B* and *SI Appendix*, Fig. S4*A*). To further confirm that SARS-CoV-2 activates CAD, we performed tracing experiments using SARS-CoV-2–infected Caco-2 cells with isotope-labeled [^{15}N-amide]glutamine and determined the intracellular concentrations of dihydroorotate, the immediate product of CAD-catalyzed reactions (Fig. 3*A*), and other downstream products, including UMP, UDP, and UTP. As shown in Fig. 3*C*, SARS-CoV-2 infection increased [^{15}N]-labeled (M+1) dihydroorotate, UMP, UDP, and UTP. Furthermore, CAD depletion in Caco-2 cells (Fig. 3*D*) abolished the increase in dihydroorotate in SARS-CoV-2–infected cells compared to control knockdown cells (Fig. 3*E*). Taken together, these results demonstrate that SARS-CoV-2 activates CAD to promote de novo pyrimidine synthesis.

To determine the role of CAD in SARS-CoV-2 infection, we depleted CAD expression in Caco-2 cells (Fig. 3*F*) and assessed viral replication by real-time PCR for viral gene expression and plaque assay for viral titer. CAD depletion reduced SARS-CoV-2 RNA abundance by ∼80% for *RdRp* and *S* genes, and ∼67% for *E* gene (Fig. 3*G*). Plaque assay further showed that CAD depletion reduced viral titer by sixfold at 72 hpi (Fig. 3*H*). Similar results were obtained in SARS-CoV-2–infected Calu-3 (*SI Appendix*, Fig. S4 *B–D*) and NHBE cells (*SI Appendix*, Fig. S4 *E–G*). Thus, CAD depletion impedes SARS-CoV-2 replication.

Nsp9 Activates CAD to Promote De Novo Pyrimidine Synthesis. In addition to the protein-deamidating activity, we determined CAD activity in de novo pyrimidine synthesis in cells with Nsp9 expression. Immunoblotting analysis revealed that Nsp9 expression robustly elevated S1859 phosphorylation of CAD, while ORF7a and other CAD-binding viral proteins had no apparent effect, in Caco-2 cells (Fig. 4*A* and *SI Appendix*, Fig. S5*A*). Next, we performed liquid chromatography–mass spectrometry (LC-MS) analysis to measure intracellular metabolites, specifically those of the central carbon metabolism and nucleotide synthesis that are relevant to CAD activities. The pool size of the metabolites of the PPP, purine, and pyrimidine pathways was increased in Nsp9-expressed Caco-2 cells (*SI Appendix*, Fig. S5 *B* and *C*). To further determine the activity of CAD in de novo pyrimidine synthesis, we performed tracing experiments using [^{15}N-amide]-glutamine. Consistent with Nsp9 elevating S1859 phosphorylation of CAD, tracing analysis showed that Nsp9 expression increased the labeled (M+1) dihydroorotate, UMP, and UDP (Fig. 4*E*). These results indicate that Nsp9 activates CAD to promote de novo pyrimidine synthesis. To probe the role of CAD in Nsp9-induced metabolic activation, we depleted CAD expression via shRNA-mediated knockdown (Fig. 4*C*) and performed tracing experiments for metabolites downstream of CAD. While Nsp9 significantly elevated [^{15}N]-labeled dihydroorotate in wild-type cells, Nsp9 failed to do so in cells deficient in CAD expression (Fig. 4*D*). A similar pattern was observed for UMP, UDP, and UTP (Fig. 4*D*). Taken together, Nsp9 activates CAD to promote de novo pyrimidine synthesis.

Given that S6K1 directly phosphorylates S1859 of CAD (27), we queried whether Nsp9 could bind to S6K1 and enhance the interaction between S6K1 and CAD. Immunoprecipitation analysis showed that S6K1 coprecipitated with Nsp9 (*SI Appendix*, Fig. S5*D*). As such, Nsp9 expression increased the interaction between S6K1 and CAD (*SI Appendix*, Fig. S5*E*). Furthermore, treatment with an S6K1 inhibitor completely abolished Nsp9-induced RelA deamidation (*SI Appendix*, Fig. S5*F*), demonstrating that S6K1 is essential for CAD-mediated RelA deamidation induced by Nsp9. We also determined whether Nsp9 could activate components of the mTOR pathway upstream of S6K, specifically, AKT and mTOR. Immunoblotting analysis showed that Nsp9 increased CAD phosphorylation, while having no effect on the phosphorylation level of AKT and mTOR (*SI Appendix*, Fig. S5*G*). These results indicate that Nsp9 recruits S6K1 to activate CAD.

SARS-CoV-2 Nsp9 Promotes Aerobic Glycolysis and De Novo Purine Synthesis. Because CAD deamidates RelA to up-regulate the expression of key glycolytic enzymes (20), we thus determined whether Nsp9-induced RelA deamidation increases the expression of these metabolic enzymes during SARS-CoV-2 infection. Real-time PCR analysis showed that SARS-CoV-2 induced the expression of *Hk1*, *Hk2*, *Pfkm*, and *Pdk4* in MEFs, supporting the biological function of RelA deamidation (*SI Appendix*, Fig. S6*A*). Furthermore, the expression of these glycolytic genes in SARS-CoV-2–infected cells was significantly higher in RelA-DD knock-in MEFs than that in wild-type MEFs, while RelA-N64A reduced the expression of these genes compared to wild-type RelA (Fig. 5*A*). It is important to note that, although basal expression of these metabolic genes was nearly undetectable in mock-infected RelA-64A-knock-in MEFs, the expression of these genes was slightly lower in RelA-64A-knock-in

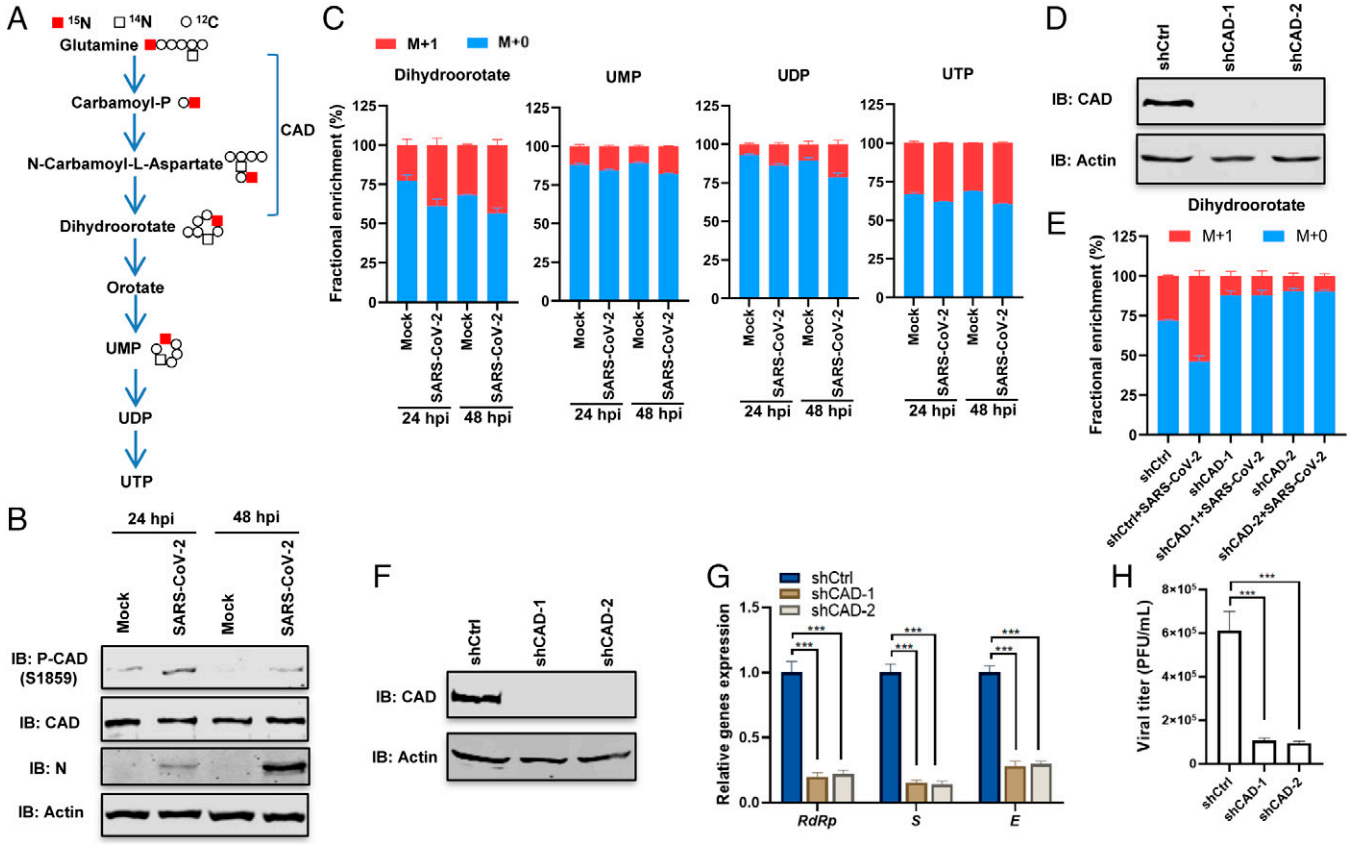

Fig. 3. SARS-CoV-2 activates CAD to promote replication. (*A*) Diagram of [^{15}N-amide]glutamine tracing for the de novo pyrimidine synthesis pathway. (*B*) Caco-2 cells were infected with SARS-CoV-2 (MOI = 5) for 24 and 48 h. WCLs were analyzed by immunoblotting with indicated antibodies. (*C*) Caco-2 cells were infected with SARS-CoV-2 (MOI = 5) for indicated hours, followed by labeling with [^{15}N-amide]glutamine for 5 min (dihydroorotate) or 45 min (UMP, UDP, and UTP). Indicated metabolites were analyzed by LC-MS. (*D* and *E*) Caco-2 cells were infected with control lentivirus or that containing shRNA against CAD. Cells were infected with SARS-CoV-2 (MOI = 1) for 96 h, followed by labeling with [^{15}N-amide]glutamine for 5 min. WCLs were analyzed by immunoblotting with indicated antibodies (*D*), while dihydroorotate was analyzed by LC-MS (*E*). (*F–H*) Caco-2 cells were infected with control lentivirus or that containing shRNA against CAD. Cells were infected with SARS-CoV-2 (MOI = 0.1) for the indicated time. WCLs were analyzed by immunoblotting with indicated antibodies (*F*). Total RNA was extracted at 72 hpi and analyzed by real-time PCR with primers specific for indicated viral genes (*G*), and viral titer was determined by plaque assay (*H*). Data are presented as means ± SD of biological triplicates (*C, E, G,* and *H*) and are representative of three independent experiments (*B, D,* and *F*). Statistical analysis was performed by the one-way ANOVA test. ***$P < 0.001$.

MEFs than wild-type MEFs when infected with SARS-CoV-2, suggesting that SARS-CoV-2 may have an alternative mechanism to up-regulate the expression of these genes. Nevertheless, these results support the conclusion that SARS-CoV-2 induces RelA deamidation to promote glycolysis. We then determined the pool size of metabolites of the central carbon metabolic pathways during SARS-CoV-2 infection. LC-MS analysis showed that SARS-CoV-2 infection in Caco-2 cells resulted in greater amounts of metabolites of the glycolysis, PPP, serine–glycine, and purine synthesis pathways (Fig. 5*B*). In general, the increase in metabolites was more pronounced in cells infected with SARS-CoV-2 at MOI = 1 than at MOI = 0.1, and at 96 hpi than at 72 hpi. Interestingly, the intracellular concentrations of ribose-5-phosphate (R5P) and ribose, key intermediates of PPP, were reduced in cells infected with SARS-CoV-2 at MOI = 1 than those infected at MOI = 0.1, which may reflect the consumption of these metabolites during robust SARS-CoV-2 replication. Similarly, SARS-CoV-2 infection also reduced the intracellular concentrations of metabolites of the pyrimidine pathway. We then performed carbon tracing analysis with isotope-labeled [U-^{13}C]glucose (Fig. 5*C*) to monitor the intermediates of the glycolysis and its branch pathway. At 72 and 96 hpi with MOI = 1, SARS-CoV-2 significantly increased labeled metabolites of the glycolysis, PPP, and purine synthesis pathways (*SI Appendix*, Fig. S6*B* and Fig. 5*D*). Next, we examined the effect of Nsp9 on the glycolysis and purine synthesis pathway. Carbon tracing analysis indicated that Nsp9 expression increased labeled G6P (M+6), 3PG (M+3), R5P (M+5), phosphoserine, and IMP (M+5) in Calu-3 cells (*SI Appendix*, Fig. S6*C*), supporting that Nsp9 promotes aerobic glycolysis and de novo purine synthesis. Furthermore, Nsp9 also activated glycolysis and de novo purine synthesis in Caco-2 cells, and CAD depletion abolished the increase in the metabolites induced by Nsp9 (Fig. 5*E* and *SI Appendix*, Fig. S6*D*). Taken together, Nsp9 promotes aerobic glycolysis and de novo purine synthesis in a CAD-dependent manner.

A CAD Inhibitor, 2-TCPA, Impedes SARS-CoV-2 Replication. Inhibition of CAD is expected to restore inflammatory response and deplete nucleotides in SARS-CoV-2–infected cells, thus impeding viral replication. We sought to develop small-molecule inhibitors to further validate CAD's role and provide therapeutic candidates to combat SARS-CoV-2 infection and COVID-19. Thus, we designed and synthesized a series of analogs of the substrate glutamine to inhibit CAD. With a reporter-based screen and several rounds of improvement via synthetic chemistry, we identified 2-TCPA as the most potent inhibitor of CAD to restore NF-κB activation (Fig. 6*A* and *SI Appendix*, Fig. S7*A*). Furthermore, 2-TCPA efficiently inhibited RelA deamidation in Caco-2 cells expressing Nsp9 (Fig. 6*B*). Consistently, 2-TCPA increased the expression of NF-κB–responsive genes, such as *IL-6*, *IL-8*, and *CCL5*, in a dose-dependent manner in HEK293T cells

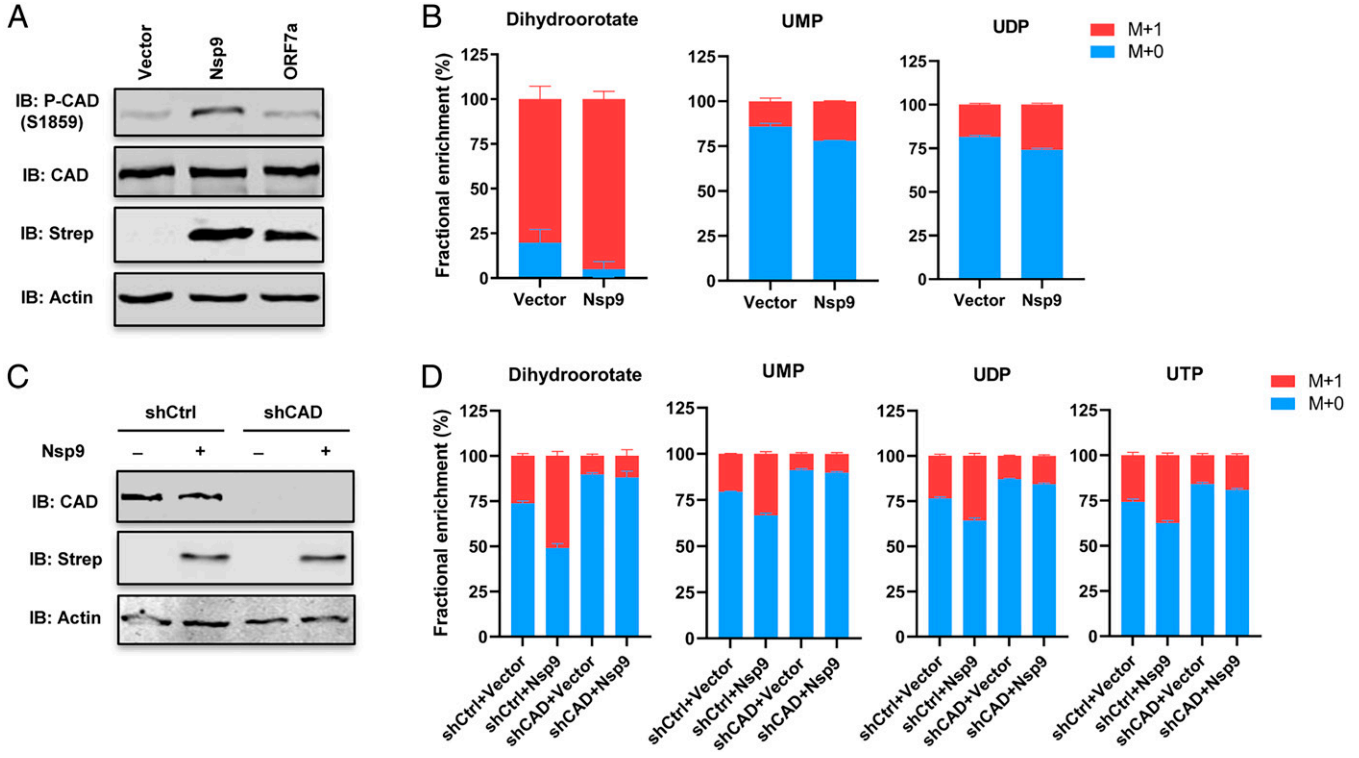

Fig. 4. SARS-CoV-2 Nsp9 activates CAD to promote pyrimidine synthesis. (*A*) Caco-2 cells were infected with control lentivirus or that carrying Nsp9 or ORF7a. At 72 hpi, WCLs were analyzed by immunoblotting with indicated antibodies. (*B*) Control or Nsp9-expressing Caco-2 cells were traced with [^{15}N-amide]glutamine for 10 min (dihydroorotate) or 1 h (UMP and UDP). Indicated metabolites were determined by LC-MS. (*C* and *D*) Caco-2 cells were infected with control lentivirus or that expressing CAD shRNA. Cells were then infected with control lentivirus carrying empty vector or Nsp9 for 96 h, followed by labeling with [^{15}N-amide]glutamine for 5 min (dihydroorotate) or 45 min (UMP, UDP, and UTP). WCLs were analyzed by immunoblotting with indicated antibodies (*C*), and indicated metabolites were analyzed by LC-MS (*D*). Data are presented as means ± SD of biological triplicates (*B* and *D*) and are representative of three independent experiments (*A* and *C*).

infected with Sendai virus (Fig. 6*C*). The increased expression of *IL-8* and *IL-6* correlated with their production in the medium analyzed by ELISA (Fig. 6*D*). 2-TCPA also greatly elevated *TNFA*, *NFKB1A*, and *CCL5* expression in SARS-CoV-2–infected Calu-3 cells (Fig. 6*E*). To determine the specificity of 2-TCPA, we showed that 2-TCPA had no effect on Sendai virus–induced *IFNB1* expression (*SI Appendix*, Fig. S7*B*) and on *IL-8* expression in CAD-KO HEK293T cells infected with Sendai virus (*SI Appendix*, Fig. S7*C*). In conclusion, 2-TCPA inhibits CAD to elevate the expression of NF-κB–responsive genes.

Next, we examined metabolites of nucleotide synthesis pathways. In Caco-2 cells treated with 2-TCPA, we found that metabolites of the PPP and pyrimidine pathway were reduced (*SI Appendix*, Fig. S7*D*). Furthermore, tracing analysis with [U-^{13}C]glucose or [^{15}N-amide]glutamine showed that 2-TCPA abolished the increase in metabolites of the glycolysis, PPP, purine, and pyrimidine pathways induced by SARS-CoV-2 (Fig. 6 *F* and *G*). These results show that 2-TCPA blocks nucleotide synthesis during SARS-CoV-2 infection.

To further characterize the antiviral activity of 2-TCPA, we first determined the effect of 2-TCPA on SARS-CoV-2 replication in Caco-2 cells. The 2-TCPA inhibited SARS-CoV-2 with a concentration that inhibits response by 50% (IC_{50}) of 2.36 μM and an IC_{90} of 7.94 μM as analyzed by plaque assay (Fig. 6*H*). Notably, 2-TCPA demonstrated no detectable cytotoxicity in Caco-2 cells up to 64 μM (Fig. 6*H* and *SI Appendix*, Fig. S7*E*). Furthermore, 2-TCPA reduced viral RNA transcripts in a dose-dependent manner and diminished N protein expression (Fig. 6*I* and *SI Appendix*, Fig. S7*F*). In Calu-3 cells, 2-TCPA demonstrated an IC_{50} of 11.61 μM and an IC_{90} of 38.53 μM on SARS-CoV-2 replication, while having no detectable cytotoxicity up to 64 μM (Fig. 6*J* and *SI Appendix*, Fig. S7*G*). Consistent with that, 2-TCPA reduced viral *S* gene expression in a dose-dependent manner (*SI Appendix*, Fig. S7*H*). We also determined the antiviral activity of 2-TCPA in NHBE, and found that 2-TCPA potently inhibited SARS-CoV-2 replication in a dose-dependent manner (*SI Appendix*, Fig. S7*I*). The 2-TCPA did not show an obvious effect on the viability and proliferation of NHBE up to 64 μM (*SI Appendix*, Fig. S7 *J* and *K*). We further evaluated whether pyrimidine supplementation could rescue SARS-CoV-2 replication in 2-TCPA–treated cells. Interestingly, uridine supplementation only minimally increased SARS-CoV-2 replication, as analyzed by plaque assay and real-time PCR in the presence of 2-TCPA (*SI Appendix*, Fig. S7*L*). Thus, 2-TCPA exerts antiviral activity partially dependent on pyrimidine inhibition. These results collectively demonstrate that 2-TCPA inhibits SARS-CoV-2 replication without obvious cytotoxicity.

Antiviral Activity of 2-TCPA against SARS-CoV-2 in Mouse Models. To further characterize the antiviral activity of 2-TCPA, we used two well-established mouse models for SARS-CoV-2 infection, that is, AAV-hACE2 (Fig. 7*A*) and K18-hACE2 transgenic mice (Fig. 7*E*) (21, 30, 31). AAV-hACE2–transduced mice were infected with SARS-CoV-2 (5×10^5 plaque-forming units [pfu]) intranasally with treatment of vehicle or 2-TCPA (20 mg/kg) daily. When mice were euthanized at 4 dpi, plaque assay using lung lysates demonstrated that 2-TCPA reduced SARS-CoV-2 load by more than three orders of magnitude (Fig. 7*B*). Similarly, real-time PCR analysis showed that 2-TCPA lowered the abundance of SARS-CoV-2 RNA by approximately three orders of magnitude (Fig. 7*C*). Conversely, 2-TPCA elevated the expression of NF-κB–dependent genes by a factor of 2 to 7 (Fig. 7*D*). These results clearly

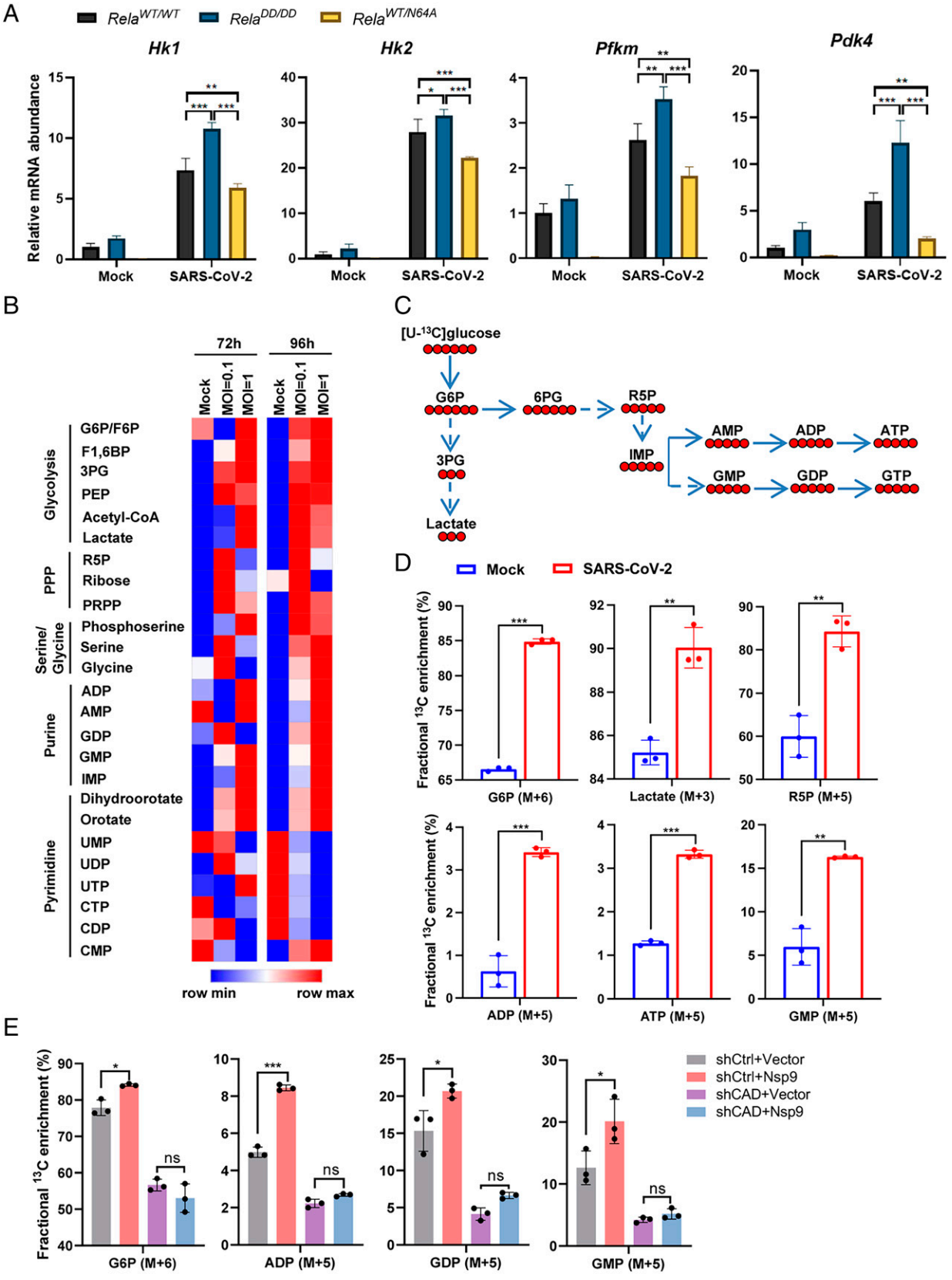

Fig. 5. SARS-CoV-2 Nsp9 promotes aerobic glycolysis and de novo purine synthesis. (*A*) RelA wild-type, RelA-DD, and RelA-N64A knock-in MEFs expressing hACE2 were infected with SARS-CoV-2 (MOI = 0.1) for 24 h. Indicated genes were analyzed by real-time PCR. (*B*) A heatmap showing the abundance of metabolites of indicated pathways in SARS-CoV-2–infected Caco-2 cells (MOI = 0.1 or 1). (*C*) Diagram of [U-^{13}C]glucose tracing for the glycolysis pathway, PPP, and purine de novo synthesis pathway. (*D*) Caco-2 cells were infected with SARS-CoV-2 (MOI = 1) for 96 h, followed by labeling with [U-^{13}C]glucose for 1 h. Indicated metabolites were determined by LC-MS. (*E*) Control or CAD-knockdown Caco-2 cells were infected with control lentivirus or that carrying Nsp9. At 96 hpi, cells were traced with [U-^{13}C]glucose for 5 min (G6P) or 2 h (ADP, GDP, and GMP) and harvested for metabolite determination by LC-MS. Data are presented as means ± SD of biological triplicates. Statistical analysis was performed by the one-way ANOVA test or unpaired, two-tailed Student's *t* test. **P* < 0.05; ***P* < 0.01; ****P* < 0.001.

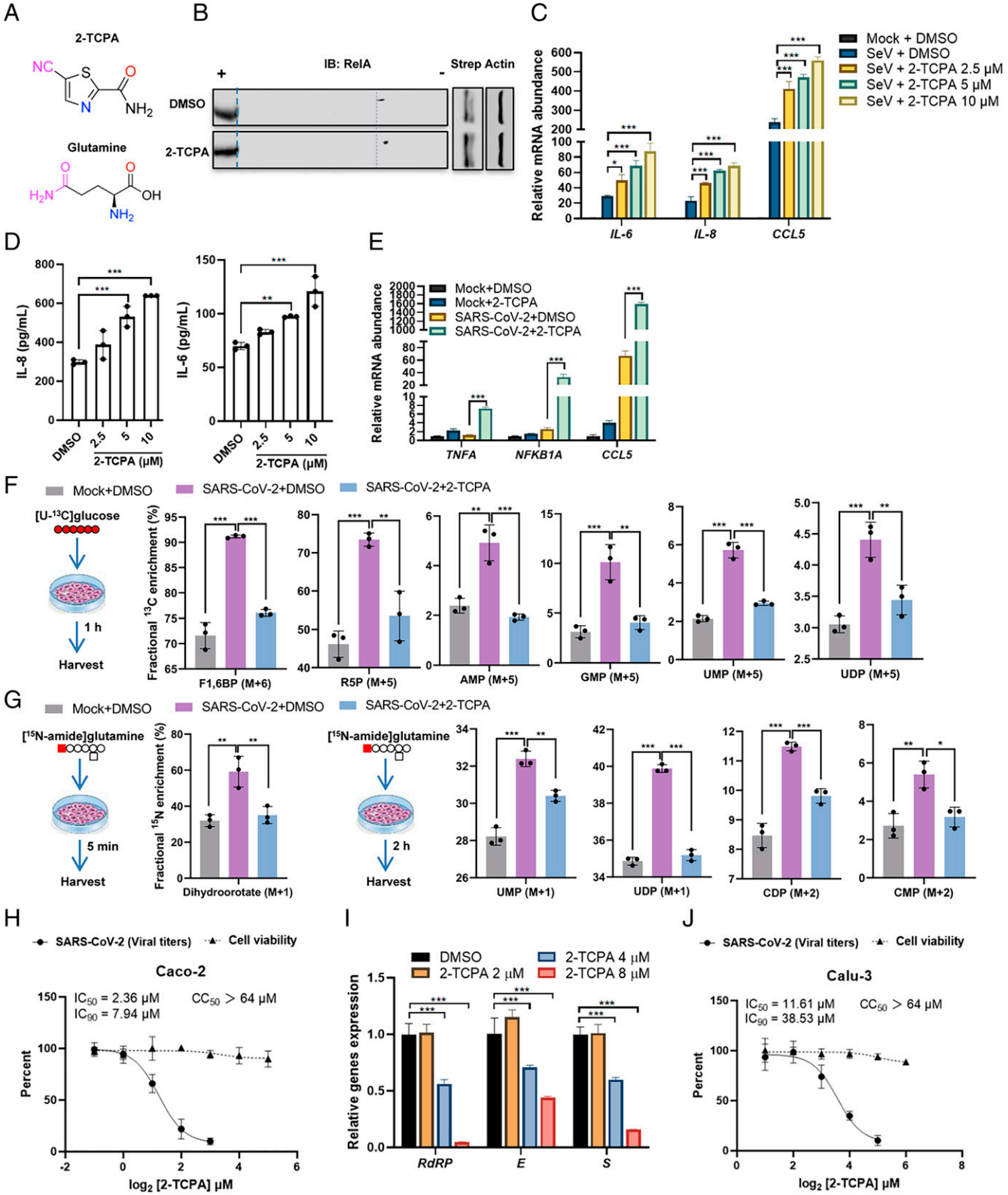

Fig. 6. CAD inhibitor 2-TCPA suppresses SARS-CoV-2 replication. (*A*) Structures of 2-TCPA and glutamine. (*B*) Caco-2 Nsp9 stable cells were treated with 4 μM 2-TCPA for 24 h. WCLs were analyzed by 2-DGE and immunoblotting. (*C*) HEK293T cells were treated with dimethyl sulfoxide (DMSO) or 2-TCPA, and infected with SeV for 6 h. Total RNA was extracted and analyzed by real-time PCR with primers specific for indicated genes. (*D*) HEK293T cells were treated with DMSO or 2-TCPA, and infected with SeV for 12 h. IL-8 and IL-6 protein levels in the medium were determined by ELISA. (*E*) Calu-3 cells were treated with DMSO or 2-TCPA (32 μM), and infected with SARS-CoV-2 (MOI = 0.1) for 96 h. Total RNA was extracted and analyzed by real-time PCR with primers specific for indicated genes. (*F* and *G*) DMSO or 2-TCPA (4 μM) treated Caco-2 cells were infected with SARS-CoV-2 (MOI = 0.1) for 72 h and then traced with [U-^{13}C]glucose (*F*) or [^{15}N-amide]glutamine (*G*) for the indicated time. Indicated metabolites were determined by LC-MS. (*H* and *J*) Caco-2 cells (*H*) and Calu-3 cells (*J*) were treated with indicated concentrations of 2-TCPA. IC_{50}, IC_{90}, and CC_{50} were calculated and are shown above the curves. All cells were pretreated for 2 h and maintained with the compound throughout the experiment. Viral titer and cell viability were determined at 72 h after treatment. (*I*) The abundance of indicated viral RNAs was determined by real-time PCR in SARS-CoV-2–infected Caco-2 cells that were treated with DMSO or indicated concentrations of 2-TCPA. Data are presented as means ± SD of biological triplicates (*C*–*J*) and are representative of three independent experiments (*B*). Statistical analysis was performed by the one-way ANOVA test. *$P < 0.05$; **$P < 0.01$; ***$P < 0.001$.

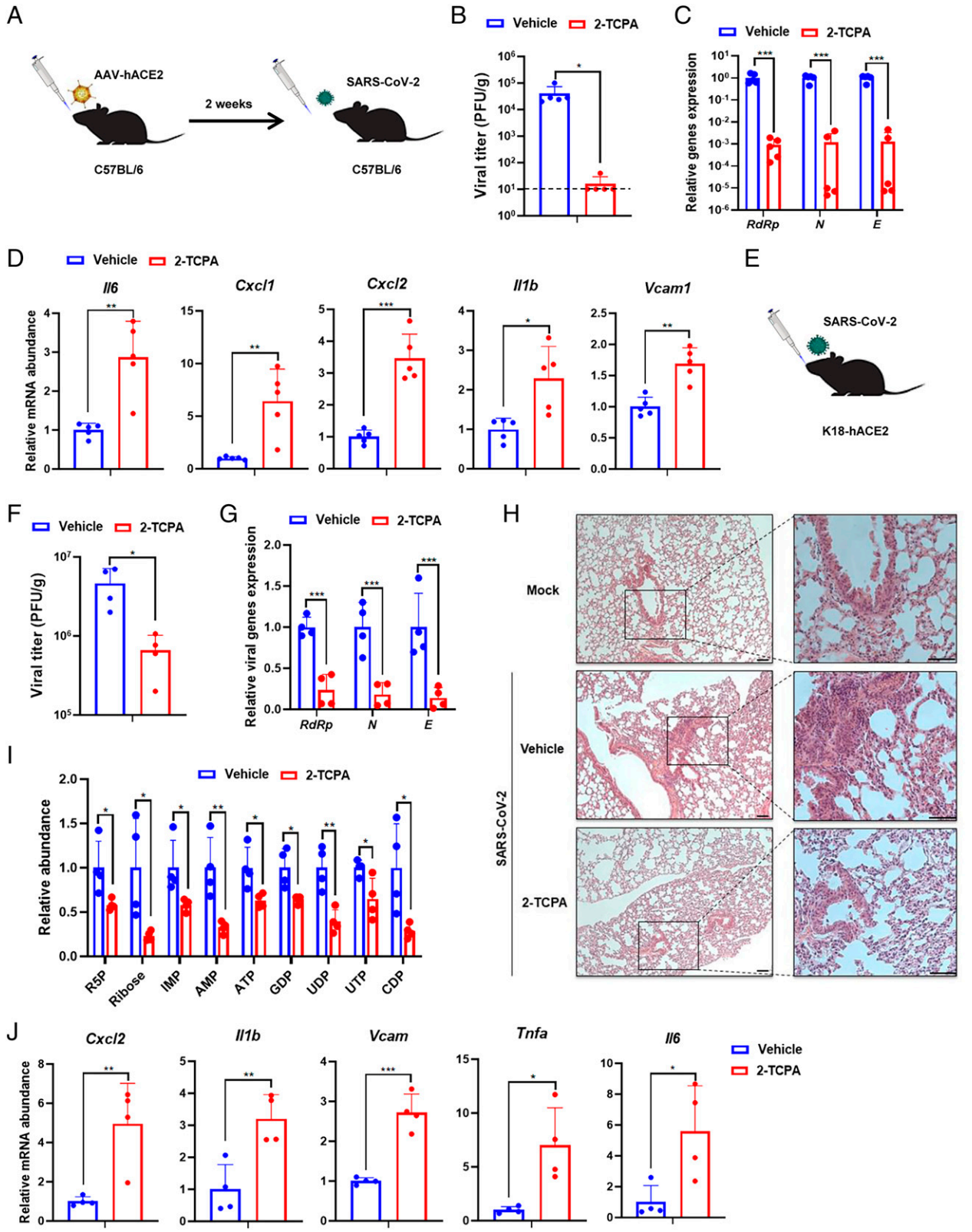

Fig. 7. The 2-TCPA inhibits SARS-CoV-2 replication in vivo. (*A*) Schematic presentation of the AAV-hACE2 transduced mouse model for SARS-CoV-2 infection. (*B–D*) AAV-hACE2 transduced mice ($n = 5$) were intranasally infected with SARS-CoV-2 (5×10^5 pfu). A dosage of 20 mg·kg^{-1}·d^{-1} of 2-TCPA or vehicle was i.p. administered to these mice at 2 h before infection. All mice were euthanized at 4 dpi to collect lung tissues for analysis of virus titer (*B*), and the expression of viral genes (*C*) and cytokine genes (*D*). The limit of detection of viral titer is indicated with a dotted line in *B*. (*E*) Schematic presentation of the K18-hACE2 model of SARS-CoV-2 infection. (*F–J*) K18-hACE2 mice ($n = 4$) were intranasally infected with SARS-CoV-2 (1×10^4 pfu). A dosage of 40 mg·kg^{-1}·d^{-1} of 2-TCPA or vehicle was i.p. administered to these mice at 1 d before infection. Mice were euthanized at 3 dpi, and the lung was collected. Viral titer (*F*) and viral gene expression (*G*) were analyzed by plaque assay and real-time PCR, respectively. Lung tissues were analyzed by H&E staining (*H*). (Scale bars: *Left*, 10 μm; *Right*, 50 μm.) Indicated metabolites (*I*) and cytokine gene expression (*J*) in the lung were analyzed by LC-MS and real-time PCR, respectively. Data are presented as mean ± SD. Statistical analysis was performed by unpaired, two-tailed Student's *t* test. *$P < 0.05$; **$P < 0.01$; ***$P < 0.001$.

demonstrate that 2-TCPA boosts antiviral immune response and impedes SARS-CoV-2 replication in the AAV-hACE2 mouse model.

To determine the effect of 2-TCPA on the systemic infection of SARS-CoV-2, we employed K18-hACE2 transgenic mice for SARS-CoV-2 infection (Fig. 7*E*). Indeed, 2-TCPA reduced SARS-CoV-2 load in the lung by ∼10-fold, as analyzed by plaque assay (Fig. 7*F*), and reduced viral RNA by a range of 80 to 90%, as analyzed by real-time PCR (Fig. 7*G*), when mice were euthanized at 3 dpi. SARS-CoV-2 antigen expression analysis in the lungs by immunofluorescence microscopy also showed that 2-TCPA reduced N protein expression in both alveoli and bronchioli areas (*SI Appendix*, Fig. S8*A*). Hematoxylin & eosin (H&E) staining showed that SARS-CoV-2 infection induced apparent inflammation within the parabronchial region that also extended to surrounding regions, compared to mock-infected mice, whereas mice treated with 2-TCPA were protected from these effects (Fig. 7*H* and *SI Appendix*, Fig. S8*B*). The lungs of SARS-CoV-2–infected mice exhibited high cellularity, indicative of excessive immune infiltration and inflammation, which was better discerned under high magnifications (*SI Appendix*, Fig. S8*C*). Reduced immune infiltration in 2-TCPA–treated mice could be the consequence of inhibited viral replication. Alternatively, 2-TCPA may inhibit the activation, proliferation, and infiltration of immune cells, since nucleotides are essential for these processes. Treatment with 2-TCPA also significantly reduced metabolites of the pyrimidine synthesis pathway, including UDP, UTP, and CDP (Fig. 7*I*). By contrast, 2-TPCA elevated the expression of antiviral genes, including *Cxcl2*, *Il1b*, *Vcam*, *Tnfa*, and *Il6*, that are dependent on NF-κB activation (Fig. 7*J*). Treatment with 2-TCPA also increased the expression of *Il1b*, *Il6*, and *Tnfa* in peripheral blood mononuclear cells without stimulation or infection (*SI Appendix*, Fig. S8*D*), suggesting that 2-TCPA can increase the basal expression of NF-κB–responsive genes. Taken together, these results collectively show that 2-TPCA inhibits de novo nucleotide synthesis and restores antiviral gene expression to impede SARS-CoV-2 replication in two mouse models.

Discussion

In this study, we report that SARS-CoV-2 activates the de novo pyrimidine synthesis pathway to fuel viral replication and, unexpectedly, to evade antiviral inflammatory response. Mechanistically, SARS-CoV-2 deploys Nsp9 to activate CAD to boost de novo pyrimidine synthesis. Concomitantly, CAD demonstrates intrinsic enzyme activity in deamidating RelA to inhibit NF-κB–dependent gene expression (20). Genetic depletion and pharmacological inhibition of CAD drained the cellular nucleotide pool and restored antiviral inflammatory response, thus effectively impeding SARS-CoV-2 replication in cultured cells and model animals. We have recently reported that CAD-mediated deamidation shunts RelA from mediating inflammatory response to aerobic glycolysis, thereby fueling cell proliferation and tumorigenesis (20). These findings support the corollary that SARS-CoV-2, like tumor cells, usurps a cellular mechanism to couple evasion of inflammatory defense response to metabolic activation.

Catalyzing the rate-limiting steps of the de novo pyrimidine synthesis pathway, CAD represents one of the key nodes of metabolic reprogramming in cell proliferation and viral replication. While cancer cells up-regulate CAD expression via gene amplification, epigenetic modifications, or posttranslational mechanisms (27–29, 32, 33), how viruses manipulate CAD-mediated pyrimidine synthesis is not known. Here we found that SARS-CoV-2 activates CAD via S6K1-mediated phosphorylation. Specifically, SARS-CoV-2 Nsp9 interacts with S6K1 and CAD, thereby promoting the interaction between S6K1 and CAD. As such, Nsp9 increases S6K1-mediated S1859 phosphorylation of CAD, a marker for CAD activation. Activated CAD fuels de novo pyrimidine synthesis in Nsp9-expressing cells and SARS-CoV-2–infected cells, which was validated by metabolite profiling and stable isotope tracing analyses. This is consistent with previous studies showing that SARS-CoV-2 increases purine and pyrimidine metabolism in sera of COVID-19 patients (34, 35), and that an inhibitor of dihydroorotate dehydrogenase (DHODH) effectively reduces SARS-CoV-2 replication in cultured cells (36–38). Moreover, SARS-CoV-2 and Nsp9 also activate CAD to deamidate RelA, thus halting antiviral inflammatory response in virus-infected cells. Although Nsp9 overexpression only inhibited the expression of NF-κB–dependent antiviral genes by approximately twofold, CAD depletion increased by more than 10-fold in SARS-CoV-2–infected cells. This may stem from the basal activity of CAD in suppressing NF-κB–dependent gene expression. Alternatively, SARS-CoV-2 may deploy other viral proteins to meddle CAD-mediated inhibition of NF-κB–dependent gene expression. Furthermore, deamidated RelA activates the expression of key glycolytic enzymes to promote glycolysis, which may be more physiologically relevant to the low-oxygen conditions of COVID-19 patients. Metabolites of the glycolysis are known to provide precursors for the synthesis of macromolecules, such as amino acids, nucleotides, and lipids (39–41).

Considering the crucial role of CAD in metabolic reprogramming and innate immune evasion during SARS-CoV-2 infection, we strove to develop a small-molecule inhibitor, 2-TCPA, that structurally resembles glutamine, to antagonize CAD. The specificity of 2-TCPA for CAD is supported by several lines of evidence. First, 2-TCPA elevated inflammatory cytokine production (e.g., IL-8) driven by NF-κB activation, while having no effect on IFN-β induction that is negatively regulated by CTP synthetase 1 (42), supporting its exquisite selectivity against members of the glutamine amidotransferase family. Second, 2-TPCA elevated inflammatory cytokine production in wild-type cells, but not in cells deficient in CAD, demonstrating the CAD-dependent effect of 2-TCPA on NF-κB activation and inflammatory cytokine induction. Third, 2-TCPA treatment did not overtly alter the intracellular metabolites of the glycolysis and nucleotide synthesis pathways in Caco-2 cells. Although CAD is essential for de novo pyrimidine synthesis during cell proliferation, 2-TCPA has a CC_{50} value against Caco-2 cells that is >25-fold of its IC_{50} on SARS-CoV-2 replication, further supporting the activation of and dependency on CAD in SARS-CoV-2 infection. Finally, treatment with 2-TCPA significantly reduced metabolites of the de novo pyrimidine pathway in SARS-CoV-2–infected cells and mice. Consistent with depleting the nucleotide pool, 2-TCPA impedes SARS-CoV-2 gene expression and genome replication, translating into significantly reduced viral load in the lung. In stark contrast, 2-TCPA treatment restored antiviral cytokine gene expression in SARS-CoV-2–infected cells and mice, despite the reduced nucleotide pool. Overall, targeting CAD with small molecules offers an antiviral modality through increasing inflammatory antiviral response and depleting nucleotides. Inhibitors targeting another pyrimidine synthetic enzyme, DHODH, showed potential utility in acute myeloid leukemia and different models of viral infection, including SARS-CoV-2 (37, 38, 43, 44). However, nucleotides are essential for the activation and proliferation of immune cells during viral infection (26); inhibitors of nucleotide synthetic enzymes may impair host immune response, particularly the adaptive immunity arm that relies on activation and proliferation of T cells and B cells. Thus, treatment modality utilizing 2-TCPA and DHODH inhibitors needs to be optimized in terms

of dosage, time, and duration of targeted delivery. Notably, 2-TCPA can enhance host antiviral response in addition to halting pyrimidine synthesis compared to DHODH inhibitors, which may explain why 2-TCPA exhibits better antiviral effects than DHODH inhibitors in vivo. Additionally, combining nucleoside analogs with DHODH inhibitors synergistically inhibits SARS-CoV-2 infection in vitro and in vivo (44). Thus, exploring potential combinations of 2-TCPA with other inhibitors may provide more opportunities for antiviral applications.

Materials and Methods

Statistical Analysis. SARS-CoV-2 viruses USA-WA1/2020 and icSARS-CoV-2-mNG (45) were obtained from University of Southern California (USC) BSL3 Core and were originally gifted from BEI Resources (NR-52281) and P.-Y. Shi's laboratory at the University of Texas Medical Branch, Galveston, TX. All SARS-CoV-2–related viral propagation, infection, and titration were performed in a biosafety level 3 (BSL-3) facility (USC) in accordance to the biosafety protocols. The pLVX-EF1alpha-2XStrep-IRES-Puro plasmids containing SARS-CoV-2 viral genes were described previously and provided by Nevan J. Krogan (University of California-San Francisco) (22). All animal work was performed under strict accordance with the recommendation in the Guide for the Care and Use of Laboratory Animals of the NIH (46). The protocol was approved by the Institutional Animal Care and Use Committee of the University of Southern California (protocol number: 21190). All mice were housed in a standard pathogen-free animal facility. Detailed materials and methods are available in *SI Appendix*.

Data Availability. Isotopologue distributions from all MS isotope tracing experiments are are avaiable at https://doi.org/10.6084/m9.figshare.19820647.v1. All other study data are included in the article and/or *SI Appendix*.

ACKNOWLEDGMENTS. We thank Drs. Jae Jung and Woo-Jin Shin (Cleveland Clinic) for cell lines, and Dr. Krogan Nevan (University of California, San Francisco) for the SARS-CoV-2 expression library. This work is partly supported by grants from NIH (Grants DE027556, CA221521, and DE026003), startup funds from the Herman Ostrow School of Dentistry of USC, and USC Zumberge Epidemic and Virus Award. B.E. was supported by the NSF Graduate Research Fellowship (Program DGE 1418060). All BSL-3 work was performed within the Hastings Foundation and Wright Foundation Laboratories at USC. SARS-CoV-2 BSL3 resources were supported by a grant from the COVID-19 Keck Research Fund under Dr. Lucio Comai.

Author affiliations: [a]Section of Infection and Immunity, Herman Ostrow School of Dentistry, Department of Molecular Microbiology and Immunology, Keck School of Medicine, University of Southern California, Los Angeles, CA 90089; [b]Department of Chemistry, Dornsife College of Arts, Letters and Sciences, University of Southern California, Los Angeles, CA 90089; [c]Florida Research and Innovation Center, Cleveland Clinic, Port St. Lucie, FL 34987; [d]Department of Molecular Microbiology and Immunology, Keck School of Medicine, University of Southern California, Los Angeles, CA 90089; and [e]Mork Family Department of Chemical Engineering and Materials Science, Norris Comprehensive Cancer Center, Los Angeles, CA 90089

1. B. Hu, H. Guo, P. Zhou, Z. L. Shi, Characteristics of SARS-CoV-2 and COVID-19. *Nat. Rev. Microbiol.* **19**, 141–154 (2021).
2. N. Petrosillo, G. Viceconte, O. Ergonul, G. Ippolito, E. Petersen, COVID-19, SARS and MERS: Are they closely related? *Clin. Microbiol. Infect.* **26**, 729–734 (2020).
3. M. M. B. Moreno-Altamirano, S. E. Kolstoe, F. J. Sánchez-García, Virus control of cell metabolism for replication and evasion of host immune responses. *Front. Cell. Infect. Microbiol.* **9**, 95 (2019).
4. E. L. Sanchez, M. Lagunoff, Viral activation of cellular metabolism. *Virology* **479–480**, 609–618 (2015).
5. S. K. Thaker, J. Ch'ng, H. R. Christofk, Viral hijacking of cellular metabolism. *BMC Biol.* **17**, 59 (2019).
6. S. Rampersad, P. Tennant, Replication and expression strategies of viruses. *Viruses* **2018**, 55–82 (2018).
7. P. V'Kovski, A. Kratzel, S. Steiner, H. Stalder, V. Thiel, Coronavirus biology and replication: Implications for SARS-CoV-2. *Nat. Rev. Microbiol.* **19**, 155–170 (2021).
8. I. Braakman, N. J. Bulleid, Protein folding and modification in the mammalian endoplasmic reticulum. *Annu. Rev. Biochem.* **80**, 71–99 (2011).
9. S. R. DeVito, E. Ortiz-Riaño, L. Martínez-Sobrido, J. Munger, Cytomegalovirus-mediated activation of pyrimidine biosynthesis drives UDP-sugar synthesis to support viral protein glycosylation. *Proc. Natl. Acad. Sci. U.S.A.* **111**, 18019–18024 (2014).
10. R. B. Chan, L. Tanner, M. R. Wenk, Implications for lipids during replication of enveloped viruses. *Chem. Phys. Lipids* **163**, 449–459 (2010).
11. A. C. Codo *et al.*, Elevated glucose levels favor SARS-CoV-2 infection and monocyte response through a HIF-1alpha/glycolysis-dependent axis. *Cell Metab.* **32**, 437–446.e5 (2020).
12. Y. Zhang *et al.*, SARS-CoV-2 hijacks folate and one-carbon metabolism for viral replication. *Nat. Commun.* **12**, 1676 (2021).
13. P. J. Mullen *et al.*, SARS-CoV-2 infection rewires host cell metabolism and is potentially susceptible to mTORC1 inhibition. *Nat. Commun.* **12**, 1876 (2021).
14. Y. Wang, M. Liu, J. Gao, Enhanced receptor binding of SARS-CoV-2 through networks of hydrogen-bonding and hydrophobic interactions. *Proc. Natl. Acad. Sci. U.S.A.* **117**, 13967–13974 (2020).
15. J. Lu, P. D. Sun, High affinity binding of SARS-CoV-2 spike protein enhances ACE2 carboxypeptidase activity. *J. Biol. Chem.* **295**, 18579–18588 (2020).
16. J. Lan *et al.*, Structure of the SARS-CoV-2 spike receptor-binding domain bound to the ACE2 receptor. *Nature* **581**, 215–220 (2020).
17. E. S. Brielle, D. Schneidman-Duhovny, M. Linial, The SARS-CoV-2 exerts a distinctive strategy for interacting with the ACE2 human receptor. *Viruses* **12**, 497 (2020).
18. S. Ozono *et al.*, SARS-CoV-2 D614G spike mutation increases entry efficiency with enhanced ACE2-binding affinity. *Nat. Commun.* **12**, 848 (2021).
19. D. Blanco-Melo *et al.*, Imbalanced host response to SARS-CoV-2 drives development of COVID-19. *Cell* **181**, 1036–1045.e9 (2020).
20. J. Zhao *et al.*, Deamidation shunts RelA from mediating inflammation to aerobic glycolysis. *Cell Metab.* **31**, 937–955.e7 (2020).
21. B. Israelow *et al.*, Mouse model of SARS-CoV-2 reveals inflammatory role of type I interferon signaling. *J. Exp. Med.* **217**, e20201241 (2020).
22. D. E. Gordon *et al.*, A SARS-CoV-2 protein interaction map reveals targets for drug repurposing. *Nature* **583**, 459–468 (2020).
23. X. Li *et al.*, SARS-CoV-2 ORF10 suppresses the antiviral innate immune response by degrading MAVS through mitophagy. *Cell. Mol. Immunol.* **19**, 67–78 (2022).
24. S. Rabinovich *et al.*, Diversion of aspartate in ASS1-deficient tumours fosters de novo pyrimidine synthesis. *Nature* **527**, 379–383 (2015).
25. W. T. Shoaf, M. E. Jones, Uridylic acid synthesis in Ehrlich ascites carcinoma. Properties, subcellular distribution, and nature of enzyme complexes of the six biosynthetic enzymes. *Biochemistry* **12**, 4039–4051 (1973).
26. Y. Ariav, J. H. Ch'ng, H. R. Christofk, N. Ron-Harel, A. Erez, Targeting nucleotide metabolism as the nexus of viral infections, cancer, and the immune response. *Sci. Adv.* **7**, eabg6165 (2021).
27. I. Ben-Sahra, J. J. Howell, J. M. Asara, B. D. Manning, Stimulation of de novo pyrimidine synthesis by growth signaling through mTOR and S6K1. *Science* **339**, 1323–1328 (2013).
28. A. M. Robitaille *et al.*, Quantitative phosphoproteomics reveal mTORC1 activates de novo pyrimidine synthesis. *Science* **339**, 1320–1323 (2013).
29. L. M. Graves *et al.*, Regulation of carbamoyl phosphate synthetase by MAP kinase. *Nature* **403**, 328–332 (2000).
30. J. Zheng *et al.*, COVID-19 treatments and pathogenesis including anosmia in K18-hACE2 mice. *Nature* **589**, 603–607 (2021).
31. E. S. Winkler *et al.*, SARS-CoV-2 infection of human ACE2-transgenic mice causes severe lung inflammation and impaired function. *Nat. Immunol.* **21**, 1327–1335 (2020).
32. K. E. Boyd, P. J. Farnham, Myc versus USF: Discrimination at the cad gene is determined by core promoter elements. *Mol. Cell. Biol.* **17**, 2529–2537 (1997).
33. S. Mannava *et al.*, Direct role of nucleotide metabolism in C-MYC-dependent proliferation of melanoma cells. *Cell Cycle* **7**, 2392–2400 (2008).
34. N. Xiao *et al.*, Integrated cytokine and metabolite analysis reveals immunometabolic reprogramming in COVID-19 patients with therapeutic implications. *Nat. Commun.* **12**, 1618 (2021).
35. B. Shen *et al.*, Proteomic and metabolomic characterization of COVID-19 patient sera. *Cell* **182**, 59–72.e15 (2020).
36. F. Hahn *et al.*, IMU-838, a developmental DHODH inhibitor in phase II for autoimmune disease, shows anti-SARS-CoV-2 and broad-spectrum antiviral efficacy in vitro. *Viruses* **12**, 1394 (2020).
37. R. Xiong *et al.*, Novel and potent inhibitors targeting DHODH are broad-spectrum antivirals against RNA viruses including newly-emerged coronavirus SARS-CoV-2. *Protein Cell* **11**, 723–739 (2020).
38. J. Luban *et al.*, The DHODH inhibitor PTC299 arrests SARS-CoV-2 replication and suppresses induction of inflammatory cytokines. *Virus Res.* **292**, 198246 (2021).
39. M. G. Vander Heiden, L. C. Cantley, C. B. Thompson, Understanding the Warburg effect: The metabolic requirements of cell proliferation. *Science* **324**, 1029–1033 (2009).
40. R. J. DeBerardinis, J. J. Lum, G. Hatzivassiliou, C. B. Thompson, The biology of cancer: Metabolic reprogramming fuels cell growth and proliferation. *Cell Metab.* **7**, 11–20 (2008).
41. J. Zhu, C. B. Thompson, Metabolic regulation of cell growth and proliferation. *Nat. Rev. Mol. Cell Biol.* **20**, 436–450 (2019).
42. Y. Rao *et al.*, Targeting CTP synthetase 1 to restore interferon induction and impede nucleotide synthesis in SARS-CoV-2 infection. bioRxiv [Preprint] (2021). https://doi.org/10.1101/2021.02.05.429959. Accessed 31 May 2022.
43. D. B. Sykes, The emergence of dihydroorotate dehydrogenase (DHODH) as a therapeutic target in acute myeloid leukemia. *Expert Opin. Ther. Targets* **22**, 893–898 (2018).
44. D. C. Schultz *et al.*, Pyrimidine inhibitors synergize with nucleoside analogues to block SARS-CoV-2. *Nature* **604**, 134–140 (2022).
45. X. Xie *et al.*, An infectious cDNA clone of SARS-CoV-2. *Cell Host Microbe* **27**, 841–848.e3 (2020).
46. National Research Council, *Guide for the Care and Use of Laboratory Animals* (National Academies Press, ed. 8, 2011).